Poroviscoelastic finite element model including continuous fiber distribution for the simulation of nanoindentation tests on articular cartilage

M. Taffetani[a,*], *M. Griebel*[b], *D. Gastaldi*[a], *S.M. Klisch*[b], *P. Vena*[a,c]

[a]*Department of Chemistry, Materials and Chemical Engineering, Laboratory of Biological Structure Mechanics (LaBS), Politecnico di Milano, Milano, Italy*

[b]*Mechanical Engineering Department, California Polytechnic State University, San Luis Obispo, USA*

[c]*IRCCS, Istituto Ortopedico Galeazzi, Milano, Italy*

Received 12 July 2013
Received in revised form
30 November 2013
Accepted 2 December 2013 Available online 12 December 2013

*Corresponding author at: Piazza Leonardo da Vinci 32, 20133 Milano (MI), Italy. Tel.: +39 022 399 4286.
E-mail address: matteo.taffetani@polimi.it (M. Taffetani).

1. Introduction

Articular cartilage (AC) is a connective tissue that covers the surface of articular joints with a thickness varying from 0.5 mm to 5 mm (Ateshian et al., 1991). Its macroscopic properties come from its hierarchical and highly ordered organization (Mow et al., 1992).

At the microscale level (10^{-7}–10^{-6} m), the biochemistry and structural organization of AC are regulated by chondrocytes, the sole type of cell existent in AC tissue that does not play a substantial mechanical role if compared to the other constituents, especially for adult tissue (Silver et al., 2003). The extracellular matrix defines the porous skeleton of the tissue and it is composed by a network of collagen (COL) and proteoglycan (PGs) molecules.

COL contributes up to ~80% of the dry weight and is almost uniformly distributed throughout the tissue, except for the superficial layers in which it is highly packed. The large slenderness ratio (length/diameter) leads to substantial COL tension–compression asymmetry (Mow et al., 1991). PGs fill the interspaces in the COL network: they are molecules with a protein core and glycosaminoglycans (GAGs) chains and their effects are to stabilize the structure and to absorb impulsive loading by storing energy (Mow et al., 1992). Thus, the ECM is often modeled as a porous and permeable fiber reinforced matrix, constituted by two macromolecular networks: a permanent network of insoluble COL fibers, characterized by a low turnover rate (Eyre, 1980), and a soluble network of large proteoglycans, characterized by a high turnover rate (Hardingham et al., 1987).

The superficial zone is the thinnest AC zone and it is composed of two layers. A sheet of fine fibrils with low polysaccharide content and without cells covers the layer composed of ellipsoid-shaped chondrocytes arranged parallel to the surface. Chondrocyte and COL densities are very high, while GAGs content is low. COL fibrils are preferably aligned parallel to the surface, defining an interwoven network that determines its tensile and shear mechanical properties, and limits the movements of macromolecules. This zone is also characterized by the highest water content (~80% of the wet weight) (Buckwalter et al., 2005; Marondas et al., 1991). Water movement is regulated by the physical porosity (hydraulic permeability) (Ateshian and Hung, 2006) and by the hydrophilic attraction of negatively charged GAGs that produces interstitial pressure. This phenomenon is called swelling and generates a non-zero strain in the AC solid matrix in the absence of externally applied load (Narmoneva et al., 1990).

AC mechanical properties are time- and history-dependent. Viscoelasticity and poroelasticity are the two major dissipation mechanisms arising from breakage and reformation of bonds within the macromolecular network under stress and to the fluid flow through the porous microstructure (Ateshian and Hung, 2006). AC mechanical response under loading is generally dependent on both mechanisms but predominance of viscoelasticity or of poroelasticity may depend on the characteristic time and length scales involved.

The first attempt to model AC assumed it to be a monophasic, linear elastic, isotropic and homogeneous material. Elmore et al. (1963) first introduced the concept of "imperfect elasticity", for which, in air, AC does not recover completely after mechanical loading is removed. Hayes and Mockros (1971) modeled viscoelasticity through a generalized Kelvin model without accounting for the role of the fluid phase. Poroelasticity was described in the pioneering work of Biot (1941); it accounts for the solid phase displacement, u, and the relative displacement between solid and fluid phases, w, ('u–w' model) as primary variables. Terzaghi (1943) introduced the poroelastic model for soils, assuming that both the solid and fluid phases homogeneously fill the volume of the specimen and Biot (1955) extended it to 3-dimensional and anisotropic solids. Rice and Cleary (1976) provided analytical solutions for a linear homogeneous poroelastic material with compressible solid and fluid phases, highlighting two limiting conditions: drained and undrained being the long term and instantaneous response, respectively. Mixture theory models for AC vary by the number and the type of constituents: e.g. the biphasic model by Mow et al. (1980) or Almeida and Spilker (1998) in which a solid and a fluid phase are considered and the triphasic model proposed by Lai et al. (1991) and evaluated by linearization in Lu et al. (2010) that also includes the negative charge of GAGs.

Analytical solutions using poroelastic or mixture models are limited. Vandamme and Ulm (2006) derived solutions for axisymmetric indentations of isotropic, transversely isotropic and orthotropic viscoelastic materials. The solution of the confined compression test on isotropic poroelastic materials can be found in the work of Biot (1941) and revisited by Cowin and Doty (2006). Numerical approaches are, then, required when inhomogeneities and complex geometries are considered (Rice and Cleary, 1976). A wide range of numerical models are presented in the literature and have included integration of features such as poroelasticity, viscoelasticity, anisotropy, non-linearity, fiber distribution and biochemical interactions. Recent refinements used for modeling AC include the contributions of the COL network through distribution functions for COL fibrils orientations as in Shirazi et al. (2011), or the effect of the large deformations on parameters, as proposed by Ateshian and Weiss (2010) for permeability.

The role of length in the time-dependent response of AC tissue is essential for the correct identification of poroelastic and viscoelastic behaviors response of the tissues. Indeed, Huang et al. (2001) showed that the viscoelastic response is independent of the characteristic length scale; the poroelastic response, instead, depends on both mechanical properties and characteristic length of the experiment as shown by Hu et al. (2010) or in Lu et al. (2010) where creep tests on samples having different geometrical features were investigated.

Macroscopic tests including confined compression, unconfined compression, indentation, tensile and shear have shown that measured mechanical properties vary substantially due to intraspecific variability, different geometrical conditions, environmental conditions and tissue sources. In Schinagl et al. (1997) nine layers were extracted from a mature AC sample and stress relaxation tests were performed over four subsequent levels of compression. Results showed that the equilibrium compressive modulus increases with the depth from the superficial to deep zones. An analogous work was presented by Chen et al. (2001) that performed oscillatory

confined compression tests on both full-thickness samples and sliced samples of adult bovine AC. Results showed that the zero strain equilibrium modulus increases and the zero strain permeability decreases with the depth from articular surface. The properties of newborn bovine AC were studied by Ficklin et al. (2007) using confined compression, unconfined compression and torsional shear tests in order to evaluate the effect of in vitro growth. Mechanical properties were found positively correlated with the GAGs and COL concentration at all tested strain levels. Another comprehensive study on AC, from tension to compression, is given in the work of Chahine et al. (2004): they analyzed specimens extracted from the surface or the deep zones and performed unconfined compression and tensile tests, in different bath conditions. The compressive modulus was found nearly constant with strain and increasing with depth. The tensile modulus, instead, was strain-dependent: it was found highest in the superficial zone. The results indicated that there is a smooth transition between tension and compression regimes and that AC shows an orthotropic symmetry with substantial tension–compression asymmetry. DiSilvestro and Suh (2001) tested mature bovine AC explants in confined compression, unconfined compression and indentation; a biphasic poroviscoelstic model was used to fit the data.

AC has been also studied at micro- and nano-scales by means of the nanoindentation technique. Indeed, nanoindentation tests have shown their capability to test biological tissues for mechanical properties (Ebenstein and Pruitt, 2006) with a relatively simple experimental set up. This test can be applied using different indenter sizes, which allows for investigation of structures of the whole tissue and its single components (Loparic et al., 2010; Stolz et al., 2009). Nanoindentation creep or relaxation tests in a liquid environment also permit the study of time-dependent properties when AC samples are submerged in physiological saline (Li et al., 2008). From a numerical point of view, simulation of nanoindentation tests introduces more computational difficulties than classical tests at the macroscale level due to the inherent inhomogeneous stress and strain fields beneath the indenter tip.

The hypothesis of the current study is that it is possible to accurately simulate the time-dependent response of adult bovine AC to spherical nanoindentation creep tests at multiple load levels. To address this hypothesis, we propose a model for the AC time-dependent mechanical response featuring viscoelasticity, poroelasticity and swelling induced by osmotic pressure; furthermore, a continuous fiber distribution model for the COL network is used as well as a depth-dependent variation of mechanical properties.

This model is used to address three specific objectives. (1) Identification of the time-dependent constitutive parameters by fitting published experimental data on the time-dependent response in a stress relaxation unconfined compression test on adult bovine AC (Korhonen et al., 2002). (2) Validation of the constitutive model by comparing results of three experimental tests, carried out on adult bovine AC, with numerical simulations performed with the parameters obtained in aim 1. The three simulations include: (i) the time-dependent response in a stress relaxation confined compression test (Korhonen et al., 2002), (ii) the drained response of a flat punch indentation test (Korhonen et al., 2002) and (iii) the estimation of the depth-dependent distribution of effective Poisson ratio in a unconfined compression test (Wang et al., 2002). (3) Once the single set of parameters used for the validation step is found, the model is subjected to an additional fine tuning process to reproduce the experimental results of nanoindentation presented in Taffetani (2013) in which AC tissue was subjected to a multi-load spherical nanoindentation creep test.

As already stated by Wilson et al. (2005), a model that considers simultaneously both the swelling effect and the anisotropic viscoelastic collagen structure is necessary to reproduce and explain the AC behaviors across the wide range of experimental protocols studied in this work.

2. Materials and methods

2.1. *Geometrical parameters: continuous fiber distribution*

To model the COL fiber network a 3D Cartesian coordinate system is used with two Eulerian angles θ and φ that define the orientation of a unit vector $\boldsymbol{n}$ (Fig. 1a).

The COL fiber distribution function $\rho(\theta,\varphi)$ is defined by:

$$\rho(\theta,\varphi)=\frac{1}{V}\left[\left(\frac{\sin(\theta)\cos(\varphi)}{\tilde{a}}\right)^2+\left(\frac{\sin(\theta)\sin(\varphi)}{\tilde{b}}\right)^2+\left(\frac{\cos(\theta)}{\tilde{c}}\right)^2\right]^{-\beta} \tag{1}$$

where $\tilde{a}^{-\beta}$, $\tilde{b}^{-\beta}$ and $\tilde{c}^{-\beta}$ are the semi-axes of an ellipsoid and the parameter β provides a generalization of the function proposed by Ateshian et al. (2009), allowing a wider or a narrower distribution if it decreases or increases, respectively

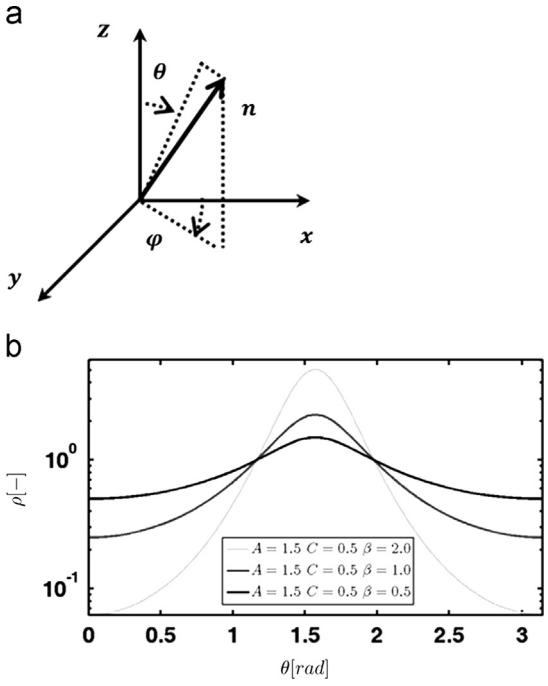

Fig. 1 – (a) 3D Cartesian coordinate system and (b) effect of parameter β on COL fiber distribution.

(Fig. 1b). V is the volume of a spherical representative volume element (RVE) of unit radius, $R = 1$:

$$V = \frac{4}{3}\pi R^3 \tag{2}$$

Since $\tilde{a}$, $\tilde{b}$ and $\tilde{c}$ have the dimensions of $(volume)^{1/2\beta}$, $\rho(\theta, \varphi)$ describes a volumetric density. In an axisymmetric COL fiber distribution model, ρ does not depend on the angle φ and Eq. (1) reduces to

$$\rho(\theta) = \frac{1}{V}\left[\left(\frac{\sin(\theta)}{\tilde{a}}\right)^2 + \left(\frac{\cos(\theta)}{\tilde{c}}\right)^2\right]^{-\beta} = \left[\left(\frac{\sin(\theta)}{A}\right)^2 + \left(\frac{\cos(\theta)}{C}\right)^2\right]^{-\beta} \tag{3}$$

where $A = \tilde{a}V^{-1/2\beta}$ and $C = \tilde{c}V^{-1/2\beta}$ are both dimensionless.

The model parameters $[A, C, \beta]$ define the distribution of the COL fibers. The overall COL fibril volume $A = \tilde{a}V^{-1/2\beta}$ can be computed by integrating Eq. (3) over the unit sphere as

$$COL_d = \int_V \rho(\theta) dV = \frac{2\pi}{3} R^3 \int_0^{\pi} \rho(\theta) \sin(\theta) d\theta \tag{4}$$

2.2. Constitutive model

COL, GAGs and MAT constituents may occupy a distinct initial configuration, κ_0^{COL}, κ_0^{GAGs} and κ_0^{MAT}, respectively; thus, three deformation gradient tensors that map each initial configuration to an intermediate tissue configuration are defined as $\mathbf{F_0^{COL}}$, $\mathbf{F_0^{GAGs}}$ and $\mathbf{F_0^{MAT}}$, respectively. This intermediate configuration is obtained by imposing an initial equilibrium step (i.e. swelling step) that allows a global tissue stress-free configuration in which COL fibers are in tension to balance the swelling pressure; moreover, the three constituents are bonded to each other, undergoing affine deformations. Therefore, it can be correctly assumed that the unique deformation gradient, $\mathbf{F}$, which maps the constituents stress-free reference configurations to the current tissue deformed configuration, takes into account the different initial configurations and it can be used for the constitutive description of the behavior of the three components separately. Considering COL, for example, the above statement means that, for each deformation gradient $\mathbf{F}^{EXP}$ related to a generic experimental condition, $\mathbf{F}$ represents $\mathbf{F}^{EXP}\mathbf{F_0^{COL}}$.

In terms of 2st Piola Kirchhoff stress $\mathbf{S}$, the MAT constituent is modeled using a Neo-Hookean material as

$$\mathbf{S^{MAT}} = \mu(\mathbf{I} - \mathbf{C^{-1}}) \tag{5}$$

where μ is the matrix shear modulus, $\mathbf{C} = \mathbf{F^T F}$ is the right Cauchy Green tensor, I is the identity tensor and superscript -1 indicates the inverse of a tensor.

Using a push forward operation, MAT Cauchy stress in current configuration, $\boldsymbol{\sigma}^{\mathbf{MAT}}$, can be derived as

$$\boldsymbol{\sigma}^{\mathbf{MAT}} = \frac{\mu}{J}(\boldsymbol{b} - \boldsymbol{I}) \tag{6}$$

where $\boldsymbol{b} = \boldsymbol{F}\boldsymbol{F}^{\mathbf{T}}$ is the left Cauchy Green tensor and $J = \det(\mathbf{F})$. The GAGs constituent is modeled using

$$\mathbf{S^{GAGs}} = -\frac{\hat{\alpha}_1}{J^{(\alpha_2 - 1)}}\mathbf{C} \tag{7}$$

where $\hat{\alpha}_1$ and α_2 are two constitutive parameters. Using a push forward operation, GAGs Cauchy stress in current configuration, $\boldsymbol{\sigma}^{\mathbf{GAGs}}$, can be derived as

$$\boldsymbol{\sigma}^{\mathbf{GAGs}} = \hat{\alpha}_1\left(\frac{1}{J}\right)^{\alpha_2}\boldsymbol{I} \tag{8}$$

where the continuity equation that relates GAGs density in reference configuration, $\rho_0^{\mathbf{GAGs}}$, and in current configuration, $\rho^{\mathbf{GAGs}}$, is used

$$\rho^{\mathbf{GAGs}} = \frac{\rho_0^{\mathbf{GAGs}}}{J} \tag{9}$$

Parameters $\hat{\alpha}_1$ and α_2 are identified using the procedure presented in Stender et al. (2012) that considered experimental swelling pressure-GAGs density relations for mature bovine AC tissue presented in Buschmann and Grodzinsky (1995). The parameter $\hat{\alpha}_1$ is related to parameter α_1 used in Stender et al. (2012) by the following relation:

$$\hat{\alpha}_1 = \alpha_1(\rho_0^{GAGs})^{\alpha_2} \tag{10}$$

The COL 2nd Piola Kirchhoff stress, $\mathbf{S^{COL}}$, is defined using the fiber distribution model. In the coordinate system presented in Fig. 1, a generic COL fiber direction in its initial configuration is defined by the unit vector $\boldsymbol{n}$ as

$$\boldsymbol{n} = \begin{bmatrix} \sin(\theta)\cos(\varphi) \\ \cos(\theta) \\ \sin(\theta)\sin(\varphi) \end{bmatrix} = \begin{bmatrix} n_1 \\ n_2 \\ n_3 \end{bmatrix} \tag{11}$$

where n_1, n_2 and n_3 are the scalar components of $\boldsymbol{n}$ along the x, y, and z axes, respectively.

Then, $\mathbf{S^{COL}}$ is defined by summing fiber stresses in all directions $\boldsymbol{n}$; the angles θ and φ belong to the domains $[0-\pi]$ and $[0-2\pi]$, respectively. In Voigt notation, the generic component of COL 2nd Piola Kirchhoff stress is obtained using

$$S_{ij}^{COL} = \int_V \overline{S}\tilde{H}(\theta, \varphi)\rho(\theta, \varphi)n_i(\theta, \varphi)n_j(\theta, \varphi)dV \tag{12}$$

where $\tilde{H}(\theta, \varphi)$ indicates a modified Heaviside function that describes a regularization function for fiber activation (presented below) and $dV = (1/3)\sin(\theta)d\theta d\varphi$ is the infinitesimal pyramidal element in which the spherical RVE can be divided. $\overline{S}$ is the fiber stress along the direction $\boldsymbol{n}$ and, in this work, is modeled as a viscoelastic response. Specifically, it is derived from the 1D integral constitutive equation for the quasi-linear viscoelastic model presented in Thomas et al. (2009)

$$\overline{S}(t) = {}^e\overline{S}(0) + \int_0^t G^{COL}(t-\tau)\frac{d^e\overline{S}}{d\tau}d\tau \tag{13}$$

The relaxation function G^{COL} is evaluated by using a Prony series of exponential terms

$$G^{COL}(t) = 1 + \sum_{i=1}^{n} g_i^{COL}\exp\left(-\frac{t}{\tau_i^{COL}}\right) \tag{14}$$

where g_i^{COL} and τ_i^{COL} are called the amplification coefficient and time constant, respectively. In this work, only one Prony series term is used. The term ${}^e\overline{S}$ describes the linear elastic COL response and it is proportional to the deformation through the constant γ

$${}^e\overline{S}(0) = \gamma\varepsilon_n \tag{15}$$

where $\varepsilon_n = n_H(\theta, \varphi)n_k(\theta, \varphi)E_{HK}$ is the strain along the direction $\boldsymbol{n}$ and E_{HK} is the appropriate scalar component of the tissue's Green Lagrange strain tensor $\boldsymbol{E} = (1/2)(\mathbf{C} - \boldsymbol{I})$. Assuming a linear elastic response for the long-term behavior of COL

Table 1 – Geometrical and constitutive parameters of the model.

Constituents	Description	Parameters
GAGs	Volumetric properties of the tissue	$\hat{\alpha}_1$, α_2: GAGs parameters in PB cell model
COL	One term Prony serie quasi-linear viscoelastic behavior	γ: elastic modulus for linear elastic response g_1^{COL}: amplification coefficient τ_1^{COL}: time constant
COL distribution	Ellipsoidal distribution	A: related to semi-axis in $\theta = \frac{\pi}{2}$ direction C: related to semi-axis in $\theta = 0$ direction β
MAT	Hyperelastic incompressible material	μ: matrix shear modulus
Permeability	Strain dependent permeability	k_0: zero strain permeability k_1: nonlinear flow limiting parameter e_0: zero strain void ratio

fibers is consistent, for example, with the model implemented in Wilson et al. (2004).

Inserting Eq. (13) in Eq. (12), the COL 2nd Piola Kirchhoff stress tensor becomes

$$S_{IJ}^{COL} = \frac{1}{3}\int_0^{2\pi}\int_0^{\pi} \overline{S}\tilde{H}(\theta,\varphi)\rho(\theta,\varphi)n_I(\theta,\varphi)n_J(\theta,\varphi)\sin(\theta)d\theta d\varphi \tag{16}$$

In an axisymmetric model, the response of the material is independent on φ. Thus, the fiber strain ε_n can be computed using $\boldsymbol{n}_{stretch}$ (instead of $\boldsymbol{n}$) that depends only on θ:

$$\boldsymbol{n}_{stretch} = \begin{bmatrix} \sin(\theta) \\ \cos(\theta) \\ 0 \end{bmatrix} \tag{17}$$

Moreover, the fiber distribution depends on θ and Eq. (16) becomes

$$S_{IJ}^{COL} = \frac{1}{3}\int_0^{2\pi}\int_0^{\pi} \overline{S}\tilde{H}(\theta)\rho(\theta)n_I(\theta)n_J(\theta)\sin(\theta)d\theta d\varphi \tag{18}$$

The double integral in Eq. (18) is now separable and it can be written as

$$S_{IJ}^{COL} = \frac{1}{3}\overline{S}\int_0^{2\pi}\Gamma(\varphi)d\varphi\int_0^{\pi}\tilde{H}(\theta)\rho(\theta)\Psi(\theta)\sin(\theta)d\theta \tag{19}$$

where $\Gamma(\varphi)$ and $\Psi(\theta)$ are functions depending on the direction chosen. Due to the axisymmetric assumption the first integral in Eq. (19) has an analytical solution for any generic φ; e.g., an example with component S_{12}^{COL} follows. By using Eq. (17) to represent n_1 and n_2, Eq. (18) becomes

$$\begin{aligned} S_{IJ}^{COL} &= \frac{1}{3}\int_0^{2\pi}\int_0^{\pi} \overline{S}\tilde{H}(\theta)\rho(\theta)\sin(\theta)\cos(\varphi)\sin(\theta)d\theta d\varphi \\ &= \frac{1}{3}\overline{S}\int_0^{2\pi}\Gamma(\varphi)d\varphi\int_0^{\pi}\tilde{H}(\theta)\rho(\theta)\Psi(\theta)\sin(\theta)d\theta \end{aligned} \tag{20}$$

where $\Gamma(\varphi) = \cos^2(\varphi)$ and $\Psi(\theta) = \sin^2(\theta)$ and $\int_0^{2\pi}\cos^2(\varphi)d\varphi = \pi$.

COL Cauchy stress is obtained by applying the push forward transformation to Eq. (19); the COL stress in current configuration $\boldsymbol{\sigma}^{COL}$ is derived as

$$\boldsymbol{\sigma}^{COL} = \frac{1}{J}\mathbf{F}\mathbf{S}^{COL}\mathbf{F}^T \tag{21}$$

To complete the proposed constitutive relationship, a strain-dependent permeability function is chosen as (Ateshian et al., 1997):

$$k(\varepsilon) = k_0\exp^{-k_1\varepsilon} \tag{22}$$

where k_0 defines the zero strain permeability and k_1 describes the exponential decrease of permeability with strain ε. According to van der Voet (1997), the permeability may instead be expressed as a function of void ratio thus Eq. (22) can be expressed as follows:

$$k(e) = k_0\left(\frac{1+e}{1+e_0}\right)^{-k_1} \tag{23}$$

where e is the current void ratio and e_0 is the initial void ratio. This approach defines an isotropic void-dependent permeability. In a finite strain setting, the void ratio changes with volumetric changes in the deformation process; therefore Eq. (23) defines the permeability as a function of the volumetric strain.

In Table 1, the parameters for the constitutive relation presented above are summarized.

2.3. Numerical implementation

Eq. (13) can be discretized using the approach proposed in Thomas et al. (2009):

$$\overline{S}_{t_2} = \gamma^e\overline{S}_{t_2} + \exp\left(-\frac{\Delta t}{\tau_1^{COL}}\right)c_{t_1} + \gamma g_1^{COL}\tau_1^{COL}\left(1-\exp\left(-\frac{\Delta t}{\tau_1^{COL}}\right)\right)\left(\frac{\Delta\varepsilon_n}{\Delta t}\right) \tag{24}$$

$$\begin{aligned} c_{t_1} = {} & c_{t_0}\exp\left(-\frac{\Delta t_{old}}{\tau_1^{COL}}\right) \\ & +\gamma g_1^{COL}\tau_1^{COL}\left(1-\exp\left(-\frac{\Delta t_{old}}{\tau_1^{COL}}\right)\right)\left(\frac{\Delta\varepsilon_{n,old}}{\Delta t_{old}}\right) \end{aligned} \tag{25}$$

where t_2 is the current time, t_1 and t_0 are times at one and two previous increments, respectively; $\Delta t = t_2 - t_1$ is the actual time step, $\Delta t_{old} = t_1 - t_0$ the previous step time; $\Delta\varepsilon_n = \varepsilon_{n,t_2} - \varepsilon_{n,t_1}$ is the current increment in deformation with ε_{n,t_1} the strain at previous time and ε_{n,t_2} the strain at the current time; $\Delta\varepsilon_{n,old}$ is the previous increment in deformation. ${}^e\overline{S}_{t_2}$ is the elastic stress at current time and Eq. (24) holds for the generic angle $\overline{\theta}$.

The implementation of this constitutive model into the commercial finite element code Abaqus 6.10 (Simulia, Providence, RI, USA) requires the computation of the correct

stiffness tangent matrix; in the case of constitutive laws in total form, the consistent tangent matrix C_{ijhk} is computed through the variation of the Kirchhoff stress $\boldsymbol{\tau}$. The whole derivation, presented in Stender et al. (2012) is not reported here.

The final expression of the stiffness tangent matrix C_{ijhk} is

$$C_{ijhk} = \frac{1}{J}\left[\frac{1}{2}(\delta_{ki}\tau_{hj} + \delta_{hj}\tau_{ik} + \delta_{hi}\tau_{kj} + \delta_{kj}\tau_{ih}) + C_{IJHK}F_{iI}F_{jJ}F_{hH}F_{kK}\right] = C_{ijhk}^{Co-TOT} + (C_{IJHK}^{MAT} + C_{IJHK}^{GAGs} + C_{IJHK}^{COL})F_{iI}F_{jJ}F_{hH}F_{kK} \quad (26)$$

where C_{IJHK} is the 4th order stiffness tensor in the reference configuration computed as $C_{IJHK} = \delta S_{IJ}/\delta C_{HK}$. C_{ijhk}^{Co-TOT} is the corotational part of the stiffness tangent matrix.

The previous Eqs. for constituent stresses are used to calculate the terms in the stiffness tangent matrix in Eq. (26) for the particular constitutive law used here.

The total Cauchy stress of the tissue, σ_{ij}^{TOT} is the summation of the three contributions

$$\sigma_{ij}^{TOT} = \sigma_{ij}^{COL} + \sigma_{ij}^{GAGs} + \sigma_{ij}^{MAT} \quad (27)$$

Then, in the spatial configuration, the corotational part in Eq. (26) becomes

$$C_{ijhk}^{Co-TOT} = \frac{1}{2}(\delta_{ki}\sigma_{hj}^{TOT} + \delta_{hj}\sigma_{ik}^{TOT} + \delta_{hi}\sigma_{kj}^{TOT} + \delta_{kj}\sigma_{ih}^{TOT}) \quad (28)$$

The 4th order stiffness tensor in reference configuration is derived below for the three components

$$C_{IJHK}^{MAT} = \frac{\mu}{2}\left(C_{IH}^{-1}C_{JK}^{-1} + C_{IK}^{-1}C_{JH}^{-1}\right) \quad (29)$$

$$C_{IJHK}^{GAGs} = \frac{\hat{\alpha}_1}{J^{\alpha_2}}\left[(\alpha_2 - 1)C_{KH}^{-1}C_{IJ}^{-1} + C_{IH}^{-1}C_{JK}^{-1} + C_{IK}^{-1}C_{JH}^{-1}\right] \quad (30)$$

$$C_{IJHK}^{COL} = \frac{1}{2}\left({}^4M_{IJHK} + DMg_{IJHK}\right) \quad (31)$$

where ${}^4M_{IJHK}$ and DMg_{IJHK} are two generalized tensor defined as

$${}^4M_{IJHK} = \int_0^{2\pi}\int_0^{\pi} \rho(\theta)\tilde{H}(\theta)dS^{COL}\,\sin(\theta)n_I(\theta,\varphi)n_J(\theta,\varphi)n_H(\theta,\varphi)n_K(\theta,\varphi)d\theta d\varphi \quad (32)$$

$$DMg_{IJHK} = \int_0^{2\pi}\int_0^{\pi} \rho(\theta)d\tilde{H}(\theta)\bar{S}\,\sin(\theta)n_I(\theta,\varphi)n_J(\theta,\varphi)n_H(\theta,\varphi)n_K(\theta,\varphi)d\theta d\varphi \quad (33)$$

and dS^{COL} is the numerical derivative of COL stress with respect to ε_n.

$$dS^{COL} = \gamma\left[1 + \left(\left(\frac{g_1^{COL}\tau_1^{COL}}{\Delta t}\right)\left(1 - \exp\left(\frac{\Delta t}{\tau_1^{COL}}\right)\right)\right)\right] \quad (34)$$

The fiber activation function $\tilde{H}(\theta)$ is computed for each direction $\boldsymbol{n}$ (that is, each angle θ) and it is described by the following piecewise function:

$$\begin{matrix}\tilde{H} = \tilde{H}_0 \\ d\tilde{H} = 0\end{matrix} \quad \text{if} \quad \varepsilon_n < \varepsilon_n^l \quad (35)$$

$$\begin{matrix}\tilde{H} = (1-\tilde{H}_0)\left\{\sin^2\left[\frac{\pi(\varepsilon_n - \varepsilon_n^l)}{2(\varepsilon_n^h - \varepsilon_n^l)}\right]\right\} + \tilde{H}_0 \\ d\tilde{H} = \frac{\pi(1-\tilde{H}_0)}{(\varepsilon_n^h - \varepsilon_n^l)}\sin\left[\frac{\pi(\varepsilon_n - \varepsilon_n^l)}{2(\varepsilon_n^h - \varepsilon_n^l)}\right]\cos\left[\frac{\pi(\varepsilon_n - \varepsilon_n^l)}{2(\varepsilon_n^h - \varepsilon_n^l)}\right]\end{matrix} \quad \text{if} \quad \varepsilon_n^l < \varepsilon_n < \varepsilon_n^h \quad (36)$$

$$\begin{matrix}\tilde{H} = 1 \\ d\tilde{H} = 0\end{matrix} \quad \text{if} \quad \varepsilon_n > \varepsilon_n^h \quad (37)$$

The values used for the simulations are: $\tilde{H}_0 = 0$, $\varepsilon_n^l = 0$ and $\varepsilon_n^h = 0.01$. This is a regularization function introduced to mitigate the strong non-linearities introduced by the on–off Heaviside function.

The built-in poroelastic implementation available in the commercial code Abaqus is used for the simulation of fluid-flow through the deformable porous matric. The non-linear viscoelastic constitutive equations presented above are implemented for the stress–strain response of the porous solid phase using a User defined MATerial (UMAT) subroutine.

2.4. *Parameter identification and validation of the constitutive model*

The model is validated through a two-step process. In the identification step, a single set of parameters able to fit the time-dependent mechanical response of unconfined compression (Korhonen et al., 2002) is identified through a trial and error procedure, allowing for the following known data: the uniaxial stress–strain relationship of each layer in the direction parallel to the surface (Charlebois et al., 2004) and the qualitative depth-dependence data of COL and GAGs contents as shown in Nieminen et al. (2001) in terms of birifrangence and optical density. The trial and error procedure is carried out on the basis of an extensive sensitivity analysis of the model with respect to each constitutive parameter presented by Taffetani (2013) and in the related work on dynamic tests presented in Taffetani et al. (2012). As an example, narrow fiber distribution around $\theta = \pi/2$ (direction parallel to the surface) results in higher undrained to drained modulus ratio; for increasing values of $\hat{\alpha}_1$, increasing swelling strain is obtained. In the validation step, the capability of this set of parameters is evaluated in simulating the time-dependent response of confined compression and the drained response of flat punch indentation, using data obtained from the same tissue source for unconfined compression (Korhonen et al., 2002), and in simulating the depth-dependent drained Poisson's ratio (Wang et al., 2002). For unconfined and confined compression, the whole stress-relaxation response is considered; for indentation, only the drained (i.e. purely elastic) response is simulated. All the experimental data used in this work are extracted from mature articular cartilage samples.

The AC sample is modeled as an axisymmetric specimen with height $h_c = 1170\ \mu m$ and radius $r_c = 1850\ \mu m$ to reproduce the geometry of the samples used for both compression tests; an additional model with height $h_i = 1170\ \mu m$ and radius $r_i = 6500\ \mu m$ is implemented to simulate the indentation test conducted with a flat punch of radius $r_p = 1500\ \mu m$. The axisymmetric models of the samples are meshed with 3600 axisymmetric 4-node elements (CAX4P) for a Soils analysis in case of the compression simulations; a mesh composed by 7200 CAX4 element, biased under the tip with a ratio of 20, is used for the indentation simulation (Fig. 2).

Since the proposed constitutive model accounts for the swelling effect of GAGs, a preliminary swelling step is modeled: this step simulates equilibration of the sample in physiological saline with no externally applied loads. Then, for the three simulations, the loading and boundary conditions used

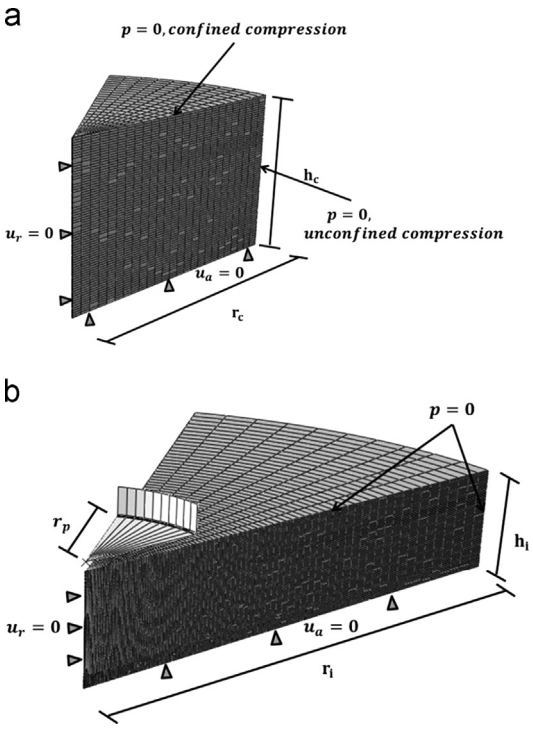

Fig. 2 – (a) 3D visualization of geometry, mesh and boundary conditions for compression tests. In both the cases, the sample is fixed in radial direction on the axis of symmetry and in axial direction on the bottom surface; the flux is allowed through the lateral surface, in case of unconfined compression, and upper surface, in case of confined compression. (b) 3D visualization of geometry, mesh and boundary condition for the sample used for flat indentation test. The sample is fixed in radial direction on the axis of symmetry and in axial direction on the bottom surface; the flux is allowed through the lateral surface and upper surface, except where the tip is in contact. Both models are axisymmetric and the choice of a 3D visualization is for sake of clarity.

experimentally are numerically reproduced: u_r describes the radial displacement, u_a the axial displacement and p the pressure. For compression, four displacement controlled steps of 5% of the initial thickness (after the swelling phase) are applied sequentially to the upper surface of the sample followed by a relaxation step to equilibrium for the same amount of time scheduled in the experiments (leading to equilibrium); the bottom surface is constrained axially ($u_a = 0$) the axis of symmetry is constrained radially ($u_r = 0$) and the fluid flow ($p = 0$) is allowed through the lateral surface (unconfined compression) or through the upper surface (confined compression). In the confined compression simulation, after the swelling phase, boundary conditions are set in order to prevent additional lateral expansion. In the indentation simulation, the displacement is applied at the tip (four steps of 5%) while the same displacement constraints for the bottom surface and the axis of symmetry are used; pressure is imposed null on the lateral and upper surfaces, except where the tip is in contact with the sample.

Following the methods of Chegini and Ferguson (2010), that used these same experimental data from compression tests to validate a biphasic fiber reinforced poroelastic model, several modeling features are adopted.

(i) All finite element models are divided into nine layers. Each layer is characterized by a stress–strain response in the radial direction having the non-linear form

$$\sigma = A_S(\exp(B_S\varepsilon) - 1) \tag{38}$$

where parameters $A_S = 6.1$ MPa and $B_S = 1.05$ correspond to the best fit obtained by Chegini and Ferguson (2010) for the experimental tensile stress σ – strain ε curves of the superficial layer shown in Charlebois et al. (2004); for the deepest layer a reduction of 62% is assumed.

(ii) The parameters used in Eq. (23) for strain-dependent permeability are $k_0 = k_0^{macro} = 5 \times 10^{-15}$ m^4/Ns and $k_1 = k_1^{macro} = 2.3$.

(iii) The depth dependent fluid volume fraction V_f based on Shapiro et al. (2001) is defined as

$$V_f = 0.9 - 0.2\left(\frac{z}{h}\right) \tag{39}$$

where z is the longitudinal coordinate and h is the sample height. By using the definition of initial void ratio e_0 one obtains the following equation for the depth-dependent initial void ratio:

$$e_0 = \frac{V_f}{(1 - V_f)} = \frac{0.9 - 0.2(z/h)}{0.1 - 0,2(z/h)} \tag{40}$$

which is a required parameter for the implementation of permeability.

Two additional assumptions on material properties are considered.

(i) The equilibrium modulus of COL fibers is defined as $\gamma = 2.7$ MPa, equal to the equilibrium modulus estimated in Wilson et al. (2005) for its standard linear solid model.

(ii) The parameter α_2 in Eq. (10) has been estimated to be 3.22, following the procedure in Stender et al. (2012).

In order to analyze the results some quantities must be defined. For unconfined and confined compression, the stress is computed as $\sigma_{d,comp} = R_{F,comp}/\pi(r_c + \Delta r_c)^2$ and the strain as $\varepsilon_{d,comp} = w/(h_c + \Delta h_c)$, where w is the upper surface displacement and Δr_c and Δh_c the increment in sample radius and height after the swelling phase. In unconfined compression Δr_c varies with w. For indentation, the stress is computed as $\sigma_{d,ind} = \kappa(R_{F,ind}/\pi r_p^2)$ and the strain as $\varepsilon_{d,ind} = w/(h_i + \Delta h_i)$, where κ is a corrective factor and Δh_i the increment in sample height after the swelling phase. As done for experimental data, the numerical stress is corrected by a factor $\kappa = 2.2$ as suggested by Hayes et al. (1972) for the geometrical situation analyzed here. Poisson's ratio is calculated as the negative ratio between the deformation in radial direction ε_r and in axial one ε_a for all the layers, i.e. $\nu_d = -\varepsilon_r/\varepsilon_a$.

2.5. *Multiload nanoindentation creep test*

Once a proper set of constitutive and geometrical parameters for bovine AC are obtained and the model is validated, the constitutive relation is used to simulate the multiload

spherical nanoindentation creep test, using the experimental protocol proposed in Taffetani (2013).

In particular, the experiment considered here refers to the case of a spherical tip of radius$R_{400} = 400\,\mu m$ and a loading rate $v_L = 1$ mN/s. The AC specimen is modeled with a radius $r_{i,400} = 3000\,\mu m$ and a height $h_{i,400} = 1170\,\mu m$. The bottom surface is constrained along the axial direction ($u_a = 0$) while the axis of symmetry along the radial direction ($u_r = 0$), fluid flow ($p = 0$) is allowed through both the upper and lateral surfaces. In the area of contact between the tip, modeled as an analytical rigid surface of radius R_{400} and the tissue, fluid flow is not allowed. In this simulation, the mesh is composed of 7200 CAX4P elements. In Fig. 3, geometry, mesh and boundary conditions are shown. The validation procedure described in the previous Section allows justifying the reliability of the model and estimating mechanical properties through the whole AC thickness for adult bovine AC. Since the results of a nanoindentation is generally affected by the material properties up to the depth of 10 times h_{max} (Karduna et al., 1997), the three most superficial layers should be included into the numerical simulation; our model accounts also for the swelling effect that is different layer by layer: therefore, it can be assumed that the behavior of each layer also affects the properties of the two layers immediately above and below. According to this consideration, we estimated that the four most superficial layers are required to correctly reproduce our results on the nanoindentation. Therefore, even if the nanoindentation finite element model includes all the nine layers, the properties of the four most superficial ones are discussed.

The overall load $F_T = 1$ mN is applied in 10 increments evenly distributed. After the preliminary swelling step, the sample is loaded to reach the first level with the prescribed loading rate; then, the load is kept constant while the displacement of the tip is monitored for 120 s (i.e. during creep); finally, the subsequent load increment is applied and the same protocol is repeated for all the levels. Consider the ten load levels j, $j = [1:1:10]$, and let F_j the jth load level, $z_{d,j}$ the indentation depth achieved at the end of the jth creep phase and $z_{i,j}$ the indentation depth achieved at the beginning of the jth creep phase (i.e. at the end of the loading phase). The drained behavior of the tissue (i.e. at equilibrium) is described by the $F_j - z_{d,j}$ data. The undrained behavior of the tissue (i.e. the short term response) is represented by the $F_j - z_{u,j}$ data, where $z_{u,j} = z_{i,j}$ if $j = 1$ and $z_{u,j} = z_{i,j} - z_{d,j-1}$ otherwise.

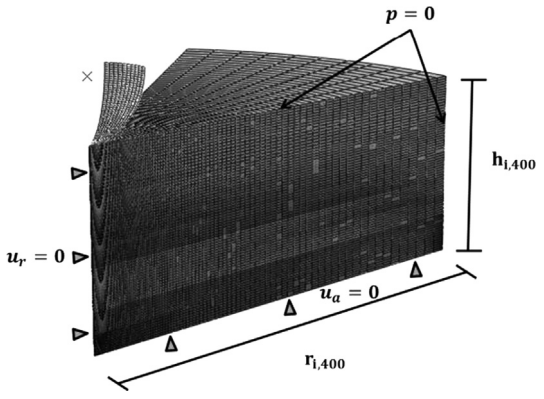

Fig. 3 – 3D visualization of geometry, mesh and boundary conditions used in the multiload nanoindentation creep test. The sample is fixed in radial direction on the axis of symmetry and in axial direction on the bottom surface; the flux is allowed through the lateral surface and upper surface, except where the tip is in contact. The choice of a 3D visualization is for sake of clarity

The described validation procedure allows justifying the reliability of the model and estimating mechanical properties through the whole AC thickness for adult bovine AC. In this second analysis, some parameters are slightly changed with respect to the set identified at macroscale, still remaining into the physiological range that AC shows experimentally. Indeed, this is justified to allow for different properties due to a different tissue source (AC from adult bovine knee but belonging to a different animal) used in the spherical nanoindentation test.

The parameters for the strain-dependent permeability are assumed on the basis of the evaluation performed in a previous study (Taffetani, 2013): $k_0 = k_0^{nano} = 3.17 \times 10^{-16}$ m^4/Ns and $k_1 = k_1^{nano} = 2.88$. To simulate nanoindentation, viscous aspects are accounted for; according to the model proposed by Wilson et al. (2004), $\tau_1^{COL} = 5$ s and $g_1^{COL} = 150$ are assumed. Parameter$\hat{\alpha}_1$ and matrix shear modulus μ are slightly tuned starting from the data found in the validation, whereas the fiber distributions are maintained the same.

To have an additional check on the parameters used for the nanoindentation test, the static shear modulus G_s obtained numerically for the four most superficial layers is compared with the experimental results of Buckley et al. (2008), in which they showed that G_s of adult bovine AC varies with depth; G_s depends not only on the matrix shear modulus μ but on the whole structure of the layers. In this work, a torsion test equivalent to the shear test proposed by Buckley et al. (2008) is applied on each of the four layers, separately: a pre-compression step of a 2.5% of the total thickness is followed by the application of an angular displacement $u_{r,3} = 0.023$ rad (equivalent of a shear strain of 2.5%). The consequent shear modulus can be computed as

$$G_s = \frac{M_t L}{J_{zz} u_{r,z}} \tag{41}$$

where L is the thickness of the specimen, M_t is the torque and $J_{zz} = (1/2)\pi r^4$ is the moment of inertia for a disk of radius r.

Table 2 summarizes the set of identified and assumed parameters; for each variable it is also reported whether it is constant or depth dependent.

3. Results

3.1. *Validation of the constitutive relationship*

The constitutive and the geometrical parameters identified for the experimental data used in the identification and validation phases are presented in Table 3 for all 9 layers.

In Fig. 4a, the nine fiber distributions identified are shown; these curves are obtained by plotting the function in Eq. (3)

Table 2 – The set of parameters subjected to identification and the set of parameters assumed from literature or previous work in both the identification/validation analysis and the application to nanoindentation. The proper references are also shown.

	Identification/validation	Nanoindentation
$\hat{\alpha}_1$ [MPa]	Identified – Depth dependent	Identified – Depth dependent
μ [MPa]	Identified – Depth dependent	Identified – Depth dependent
A [dimensionless]	Identified – Depth dependent	Imposed – Depth dependent [from validation]
C [dimensionless]	Identified – Depth dependent	Imposed – Depth dependent [from validation]
β [dimensionless]	Identified – Depth dependent	Imposed – Depth dependent [from validation]
α_2 [dimensionless]	Imposed – Constant [from Stender et al. (2012)]	Imposed – Constant [from Stender et al. (2012)]
k_0 [m^4/Ns]	Imposed – Constant [from Chegini and Ferguson (2010)]	Imposed – Constant [from Taffetani (2013)]
k_1 [dimensionless]	Imposed – Constant [from Chegini and Ferguson (2010)]	Imposed – Constant [from Taffetani (2013)]
e_0 [dimensionless]	Imposed – Depth dependent [from Shapiro et al. (2001)]	Imposed – Depth dependent [from Shapiro et al. (2001)]
γ [MPa]	Imposed – Constant [from Wilson et al. (2005)]	Imposed – Constant [from Wilson et al. (2005)]
g_1 [dimensionless]	–	Imposed – Constant [from Wilson et al. (2005)]
τ_1 [s]	–	Imposed – Constant [from Wilson et al. (2005)]

and using parameters A, C and β listed in Table 3. Superficial layers are characterized by narrow orientation distribution around $\theta = \pi/2$; whereas, deeper layers are characterized by an evenly distributed fiber orientation. In Fig. 4b, the tensile stress–strain response that is obtained by using the identified set of parameters is plotted for the first, the sixth and the ninth layers together with the limits suggested by Chegini and Ferguson (2010), up to a maximum of 10% strain. In Fig. 4c, depth-dependent functions for both $A = \tilde{a} V^{-1/2\beta}$ and $\hat{\alpha}_1$ are shown: indeed, the COL content exhibits a local minimum at about 200 μm from the surface where it start to increase towards a maximum at about 650–700 μm; the GAGs content is, instead, monotonically increasing with the depth and reaching a plateau. $A = \tilde{a} V^{-1/2\beta}$ is computed by using Eq. (4) while $\hat{\alpha}_1$ as in Table 3.

In Fig. 5a and b, the experimental and numerical reaction forces R_F in the cases of unconfined compression and confined compression are shown; numerical values were obtained using the poroelastic model. The goodness of the fit can be evaluated through the coefficient of determination: $R^2 = 0.90$ for unconfined compression and $R^2 = 0.88$ for confined compression.

In Fig. 6a, experimental and numerical values for the drained stressσ_d–strain ε_d response is shown for both the compression and the indentation tests.

In Fig. 6b, numerical values obtained in this study for the depth dependent Poisson's ratio ν_d, computed at imposed 10% of strain, is shown. Experimental results obtained by Wang et al. (2002) are also shown.

3.2. *Application to multiload nanoindentation creep test*

In Fig. 7a, experimental and numerical force–displacement data for the drained and undrained responses are presented. In Fig. 7b, three creep curves, related to three load levels (0.1 mN, 0.2 mN, 0.3 mN), are shown, compared with the mean values measured experimentally.

Nanoindentation results shown in Fig. 7 are obtained for both μ and $\hat{\alpha}_1$ increasing with depth in ranges of [0.17 – 0.25] MPa and [0.045 – 0.070] MPa, respectively. Instead of showing them separately, it is possible to analyze their effects through the matrix equivalent shear modulus G_s that can be estimated by running torsion virtual experiments (finite element model simulations) and applying Eq. (41). In Fig. 8, the values of G_s numerically computed are reported; experimental values by Buckley et al. (2008) are also reported for comparison purposes. The results consider only the four top layers.

4. Discussion and conclusion

In this study, a constituent-based poroviscoelastic constitutive model for AC is developed with the purpose of simulating the mechanical response of AC superficial layers to spherical nanoindentation tests (Taffetani, 2013).

The constitutive parameters have been identified by fitting experimental data for the time-dependent response in a stress relaxation unconfined compression test (Korhonen et al., 2002), using a set of parameters such that GAGs and COL contents, presented in Fig. 4c, are in good agreement with available experimental data (Nieminen et al., 2001). Nine sets of mechanical parameters for the nine layers of adult bovine AC sample have been identified.

The validation of the model has been achieved by simulating three independent sets of experimental data using the fitted parameter set: (i) the time-dependent response in a stress relaxation confined compression test (Korhonen et al., 2002); (ii) the drained response of a flat punch indentation test (Korhonen et al., 2002); (iii) the estimation of the depth-dependent distribution of effective Poisson ratio in a unconfined compression (Wang et al., 2002). Regarding the second data set mentioned above, the whole time dependent reaction force measured experimentally is not simulated in this work because an impervious indenter is used in the proposed model; whereas, the indentation test in Korhonen et al. (2002) have been carried out by using a permeable tip.

The nanoindentation experiments have been simulated by a further fine tuning of the parameter μ (shear modulus for the MAT) and the swelling parameter $\hat{\alpha}_1$. The results have shown that the model is able to simulate the response to nanoindentation and, in particular: the equilibrium response (drained condition), the short term response (undrained

Table 3 – Geometrical and constitutive parameters imposed and identified for the experimental data used in the validation step.

Layer	$\hat{\alpha}_1$ [MPa]	α_2 [dimensionless]	μ [MPa]	k_0 $[m^4/Ns]$	k_1 [dimensionless]	e_0 [dimensionless]	A [dimensionless]	C [dimensionless]	β [dimensionless]	γ [MPa]
1	0.005		0.005			8	4	0.11	1.6	
2	0.01		0.008			6.9	3.4	0.13	1.6	
3	0.025		0.015			6.3	3.4	0.15	1.5	
4	0.035		0.05			5.9	3.3	0.25	1.3	
5	0.042	3.22	0.08	5×10^{-15}	2.3	5.1	2.2	0.55	1.2	2.7
6	0.048		0.1			4.3	1.6	0.83	1.2	
7	0.053		0.3			3.4	1.1	1.2	1.2	
8	0.058		0.65			2.7	0.7	1.6	1.2	
9	0.06		0.8			2	0.6	1.6	1.1	

Fig. 4 – (a) Fiber distributions identified for the nine layers modeled. (b) Stress–strain relations, up to a maximum strain of 10% strain, are shown for three representative layers (the first, the sixth and the ninth) together with the limits (first and ninth layers) suggested by Chegini and Ferguson (2010). (c) Depth-dependent values of COL content, computed as in Eq. (3), and parameter $\hat{\alpha}_1$.

condition) and the time-dependent displacement data at all load levels.

Microstructural features of the tissue have been taken into account, allowing us to show that a depth-dependent distribution of tissue composition plays a relevant role in nanoindentation tests even for shallow indentation (about 20 μm). In particular, the GAGs content and MAT shear modulus as well as the COL orientation distribution functions have been identified in a layer by layer fashion, leading to an accurate simulation of both experimental macroscopic data available in literature, and spherical nanoindentation tests in the time domain presented in Taffetani (2013). Moreover, the COL orientation distributions are consistent with fibers mainly parallel to the articular surface in superficial layers and fibers mostly perpendicular to the bone in deep layers (Fig. 4a), in agreement with experimental data (Buckwalter et al., 2005).

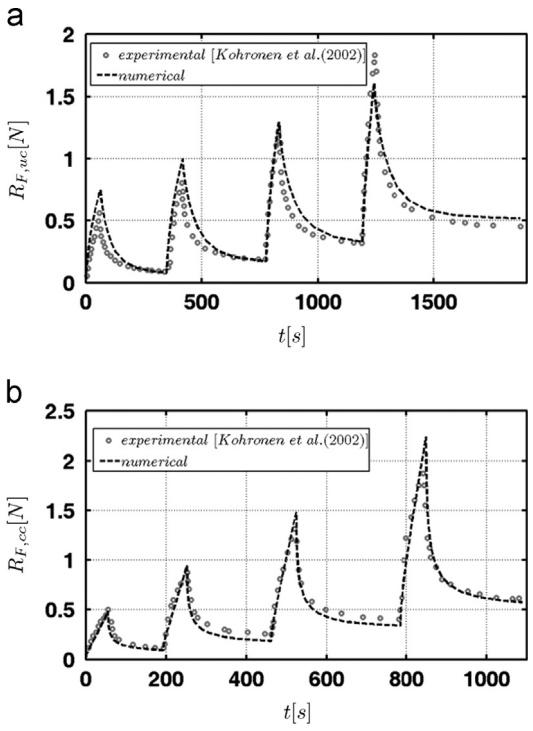

Fig. 5 – (a) Experimental numerical reaction force comparisons for (a) unconfined compression (uc) and (b) confined compression (cc) tests.

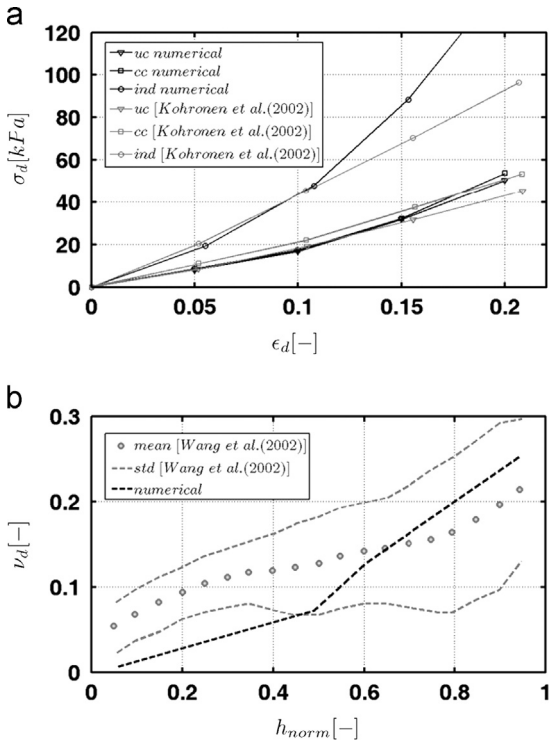

Fig. 6 – (a) Experimental (gray curves) numerical (black curves) drained stress–strain relation; triangles identify the unconfined compression test, squares the confined compression test and circles the indentation test. (b) Experimental (gray curves) numerical (black curve) Poisson's ratio measured at 10% of strain after the relaxation phase in unconfined compression.

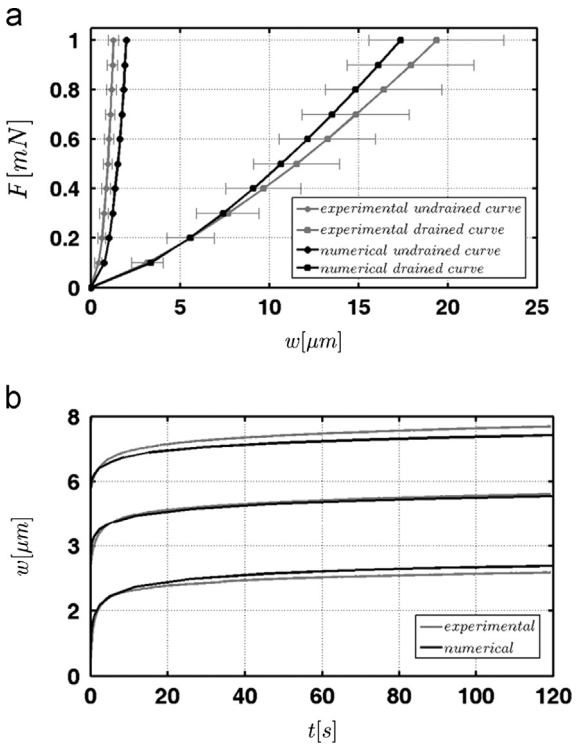

Fig. 7 – (a) Experimental and numerical results for the drained and undrained responses of the tissue; experimental data are shown with ± one standard deviation. (b) Experimental and numerical results for three representative creep curves, for the lowest three levels of load. Grey curves identify experimental mean data; black ones the numerical results.

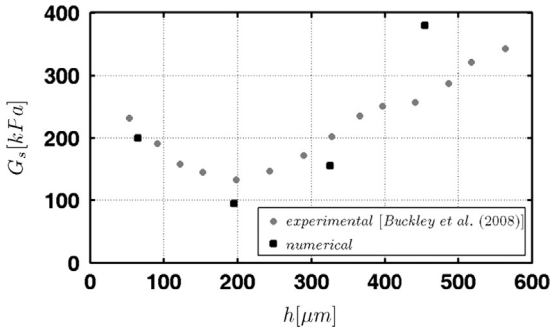

Fig. 8 – Experimental numerical values for the depth-dependent tissue shear modulus. Gray markers define experimental data whereas the black ones are numerical results.

Regarding the results at macroscale, the comparison between numerical and experimental effective Poisson's ratios is shown in Fig. 6c: the model prediction is in agreement with the experimental results, especially for deep layers. The identified GAGs swelling pressure $\hat{\alpha}_1$ parameters are such that the overall swollen geometry remains in the experimental standard deviation proposed in the work of Korhonen et al. (2002): $1400 \pm 300\ \mu m$ is the reference data while $1271\ \mu m$ is the numerical thickness obtained.

Regarding the multiload spherical nanoindentation test, a fine tuning of the matrix shear modulus μ and of the swelling parameter $\hat{\alpha}_1$ was needed: for each layer, the remaining parameters were kept fixed (see Table 2). The numerical model for the multiload nanoindentation tests successfully simulates the experimental data and this result is further corroborated by the following quantitative considerations. Chahine et al. (2005) analyzed the relationship between the swelling pressure π^{GAGs} (or osmotic pressure, equal to $\hat{\alpha}_1$) and the fixed charge density c^F (related to GAGs density) for different saline concentrations. The work of Ateshian et al. (2009), also supported by the work of Lu and Mow (2008), suggested that mature bovine AC has typical values for c^F ranged from 0.04 mEq/l to200 mEq/l. A more precise value can be found in the work of Han et al. (2011) in which the value of 100 mEq/l at 0% strain was proposed as a characteristic value for the whole AC sample. An estimation of the swelling parameter $\hat{\alpha}_1$ is obtained by entering the above values for c^F in the $c^F - \pi^{GAGs}$ curves of Chahine et al. (2005), leading to $\hat{\alpha}_1$ values ranging from 0.03 MPa to 0.1 MPa. These values are consistent with those obtained from fitting of the spherical nanoindentation tests of this study, in which $\hat{\alpha}_1$ increases with depth from 0.045 MPa to 0.070 MPa. This result is also consistent with the GAGs concentration increase with depth as found in (Buckwalter et al., 2005). Tissue shear modulus G_s, that depends also on the identified matrix shear modulus μ, is consistent with that obtained in experimental results of Buckley et al. (2008) (Fig. 8). It can be expected that spherical nanoindentation tests conducted on swelling AC tissues are affected by the material properties of the top four layers of our model. Therefore, in the case in which only the indentation depth/reaction force curve is the available experimental data, no speculation can be done regarding the deepest layers. In this 9-layers model, the properties of the top four layers may play a role in the experiment. If characterization of the deep tissue layers is sought, a more extensive nanoindentation test campaign should be planned. In particular, the use of different penetration depths and different tip radii can be an option. However, the identification process is certainly a difficult task.

Many literature studies have modeled the time-dependent properties of AC tissue. One unique feature of the present study is that it used a comprehensive model for the time-dependent response of the AC tissue which is able to simulate different loading conditions such as compression tests as well as indentation tests with flat and spherical indenters.

Seifzadeh et al. (2011) presented a porohyperviscoelastic model for AC that considers fiber remodeling via re-orientation of fiber directions, validated through a comparison with the indentation data presented by DiSilvestro and Suh (2001). The matrix was assumed viscoelastic, where the shear and bulk moduli was modeled using two Prony series with three terms each, the COL fiber distribution was considered as in (Holzapfel et al., 2006) and the permeability was modeled as strain-dependent; but, the effect of GAGs was not modeled in an explicit fashion as done in the present study. In Ateshian et al. (2009) the focus was on an elastic AC model with a continuous fiber distribution; in agreement with the results shown in our work, the fiber distribution approach appears more powerful than one using discrete fibers. Moreover, Ateshian et al. (2009) introduced the swelling of GAGs regulated by the biochemical composition of the environment in which AC is submerged; however, neither permeability nor viscous effects were accounted for. An interesting fibril reinforced model was proposed by Li et al. (1999); in that model, an incompressible elastic isotropic porous matrix was filled by incompressible fluid, and the fibrillar part was distributed along three principal directions of a cylindrical reference system. The stress–strain relationship of the fibrillar network was linear (and null in compression), whereas the permeability was exponentially decreasing with strain. No effect of GAGs was taken into account. Wilson et al. (2005) used a biphasic model in which the solid matrix consisted of a swelling non-fibrillar part and a fibrillar part representing the COL network. A total of 9 viscoelastic fibrils at each material point were used to model the superficial layers of AC using a discrete fiber approach; the used discrete distribution of fibers introduced a simplified depth dependent distribution of COL. A further discrete fiber distribution approach is presented in Pierce et al. (2009) that adapted the model proposed by Holzapfel et al. (2006) using microstructural data extracted from the imaging method proposed by Lilledahl et al. (2011). Nagel and Kelly (2012) presented a comprehensive mode for AC tissue which includes both swelling and anisotropy modeled through the structural tensor approach: this approach predicts a strain-softening response upon compression which is also shown in experimental data by Chahine et al. (2004) where the compressive elastic modulus decreases until compression strain of about 5% is reached. The collagen fiber distributed model proposed in our work can, in general, predict the stress-softening in compression. This issue has been previously discussed in Stender et al. (2012): the collagen and matrix contributions to the stress progressively decrease during compression and the critical strain at which softening ends depends on the GAGs density and COL network properties. This phenomenon was quantitatively predicted in Klisch et al. (2008) in which compression secant modulus for unconfined compression tests was reported to decrease with compression strain. Nevertheless, the compression experiments used in the identification process do not exhibit such a strain-softening because the first compression strain level (10%) overcomes the critical strain identified in Chahine et al. (2004).

Although reasonable agreement between experimental and numerical results is achieved, further improvements are required. Indeed, the Poisson's ratio computed numerically is slightly lower than experimental results in the most superficial layers and the equilibrium (drained) stress–strain response to flat indentation slightly differs for higher strains (see Fig. 6a). This limitation is likely due to the parameter identification procedure; for example, neither the fixed charge density c^F nor the depth-dependent COL fiber distribution were directly measured for the specific tissue source studied here, leading to some uncertainty in the related model parameters. This limitation can be overcome with more accurate parameter identification with additional tissue specific data that would be obtained by integrating information provided by other means of investigations like quantitative histology. This approach may lead to a substantial

improvement in the predictive capability of this model. Another limitation is the assumption of a strain-dependent isotropic permeability is another limitation of this model since anisotropic permeability (Ateshian and Weiss, 2010; Federico and Herzog, 2010) or permeability dependent on fiber direction (Pierce et al., 2010) can also play an important role that may need to be accounted for to improve the model's predictive capabilities.

The trial and error procedure used to identify material parameters does not guarantee the uniqueness of the optimal solution to the identification problem. However, the parameter values have been sought within physiologic ranges and the identified model parameters were consistent with previous studies.

The constituent-based modeling provided in this work is well suited to an approach that integrates mechanical test and depth-dependent microstructural data and may open new opportunities in integrating tissue modeling with tissue testing for diagnostic purposes. Improving our understanding of the composition–property–function interrelationship may enhance understanding of mechanisms of AC tissue disease and provide new tools for early diagnosis.

REFERENCES

Almeida, E., Spilker, R., 1998. Finite element formulations for hyperelastic transversely isotropic biphasic soft tissues. Comput. Methods Appl. Mech. Eng. 151, 513–538.

Ateshian, G., Soslowsky, L., Mow, V., 1991. Quantitation of articular surface topography and cartilage thickness in knee joints using stereophotogrammetry. J. Biomech. 24 (8), 761–776.

Ateshian, G., Warden, W., Kim, J., Grelsamer, R., Mow, V., 1997. Finite deformation biphasic material properties of bovine articular cartilage from confied compression experiments. J. Biomech. 30, 1137–1164.

Ateshian, G., Hung, C., 2006. The natural synovial joint: properties of cartilage. Proc. Inst. Mech. Eng. J.—J. Eng. 220, 657–670.

Ateshian, G., Rajan, V., Chahine, N., Canal, C., Hung, C., 2009. Modeling the matrix of articular cartilage using a continuous fiber angular distribution predicts many observed phenomena. J. Biomech. Eng. 131 (061003-1:10).

Ateshian, G., Weiss, J., 2010. Anisotropic hydraulic permeability under finite deformation. J. Biomech. Eng. 132, 111004.

Biot, M., 1941. General theory of three dimensional consolidation. J. Appl. Phys. 12, 155–164.

Biot, M., 1955. Theory of elasticity and consolidation for a porous anisotropic solid. J. Appl. Phys. 26 (2), 182–185.

Buckley, M., Glghorn, J., Bonasser, L., Cohen, I., 2008. Mapping thedepth dependence of shear properties in articular cartilage. J. Biomech. 41, 2430–2437.

Buckwalter, J., Mankin, H., Grodzinsky, A., 2005. Articular cartilage and osteoarthritis. AAOS Instr. Course Lect. 54, 465–480.

Buschmann, M., Grodzinsky, A., 1995. A molecular model of proteoglycan-associated electrostatic forces in cartilage mechanics. J. Biomech. Eng. 117, 179–192.

Chahine, N., Wang, C., Hung, C., Ateshian, G., 2004. Anisotropic strain-dependent material properties of bovine articular cartilage in the transitional range from tension to compression. J. Biomech. 37 (8), 1251–1261.

Chahine, N., Chen, F., Hung, C., Ateshian, G., 2005. Direct measurement of osmotic pressure of glycosaminoglycan solutions by membrane osmometry at room temperature. Biophys. J. 89 (3), 1543–1550.

Charlebois, M., McKee, M., Buschmann, M., 2004. Nonlinear tensile properties of bovine articular cartilage and their variation with age and depth. J. Biomech. Eng. 126, 129–137.

Chegini, S., Ferguson, S.J., 2010. Time and depth dependent Poisson's ratio of cartilage explained by an inhomogeneous orthotropic fiber embedded biphasic model. J. Biomech. 43, 1660–1666.

Chen, A., Bae, W., Schinagl, R., Sah, R., 2001. Depth- and strain-dependendent mechanical and electromechanical properties of full-thickness bovine articular cartilage in confined compression. J. Biomech. 34 (1), 1–12.

Cowin, S., Doty, S., 2006. Tissue Mechanics. Springer Verlag, New York.

DiSilvestro, M., Suh, J., 2001. A cross-validation of the biphasic poroviscoelastic model of articular cartilage in unconfined compression, indentation and confined compression. J. Biomech. 34, 519–525.

Ebenstein, D., Pruitt, L., 2006. Nanoindentation of biological materials. Nano Today 1, 26–33.

Elmore, S., Skoloff, L., Norris, G., Carmeci, P., 1963. Nature of "imperfect" elasticity of articular cartialge. J. Appl. Physiol. 18 (2), 393–396.

Eyre, D., 1980. Collagen: molecular diversity in the body's protein scaffold. Science 207, 1315–1332.

Federico, S., Herzog, W., 2010. On the anisotropy and inhomogeneity of permeability in articular cartilage. Biomech. Model Mechanobiol. 7, 367–378.

Ficklin, T., Thomas, G., Barthel, J., Thonar, E., Masuda, K., Asanbaeva, A., Thonar, E., Masuda, K., Chen, A., Sah, R., Davol, A., Klish, S., 2007. Articular cartilage mechanical and biochemical property relations before and after in vitro growth. J. Biomech. 40 (16), 3607–3614.

Han, E., Chen, S., Klisch, S., Sah, R., 2011. Contribution of proteoglycan osmotic swelling pressure to the compressive properties of articular cartilage. Biophys. J. 101 (4), 916–924.

Hardingham, T., Muir, H., Kwan, M., Lai, W., Mow, V., 1987. Viscoelastic properties of proteoglycans solutions with varying proportions present as aggregates. J. Orthop. Res. 5, 36–46.

Hayes, W., Mockros, L., 1971. Viscoelastic properties of human articular cartilage. J. Appl. Physiol. 31 (4), 562–568. Hayes, W.,

Keer, L., Herrmann, G., Mockros, L., 1972. A mathematical analysis for indentation tests of articular cartilage. J. Biomech. 5, 541–551.

Holzapfel, G., Gasser, T., Ogden, R., 2006. A new constitutive framework for arterial wall mechanics and a comparative study of material models. J. Elast. 61, 1–48.

Huang, C., Mow, V., Ateshian, G., 2001. The role of flow independent viscoelasticity in the biphasic tensile and compressive responses of articula cartilage. J. Biomech. Eng. 123 (5), 410–418.

Hu, Y., Zhao, X., Vlassak, J., Suo, Z., 2010. Using indentation to characterize the poroelasticity of gels. Appl. Phys. Lett. 96 (121904-1:3).

Karduna, A., Halperin, H., Yin, F., 1997. Experimental and numerical analyses of indentation in finite isotropic and anisotropic rubber-like materials. Ann. Biomed. Eng. 25, 1009–1016.

Klisch, S., Asanbaeva, A., Oungoulian, S., Masuda, K., Thonar, E., Davol, A., Sah, R., 2008. A cartilage growth mixture model with collagen remodeling: validation protocols. J. Biomech. Eng. 130 (3) (031006-1:11).

Korhonen, R., Laasanen, M., Toyras, J., Rieppo, J., Hirvonen, J., Helminen, H., Jurvelin, J., 2002. Comparison of the equilibrium response of articular cartilage in unconfined compression, confined compression and indentation. J. Biomech. 35, 903–909.

Lai, W., Hou, J., Mow, V., 1991. A triphasic theory for the swelling and deformation behaviors of articular cartilage. J. Biomech. Eng. 113, 245–258.

Li, L., Soulhat, J., Buschmann, M., Shirazi-Adl, A., 1999. Nonlinear analysis of cartilage in unconfined ramp compression using a fibril reinforced poroelastic model. Clin. Biomech. 14, 673–682.

Li, L., Korhonen, R., Iivarinen, J., Jurvelin, J., Herzog, W., 2008. Fluid pressure driven fibril reinforcement in creep and relaxation tests of articular cartilage. Med. Eng. Phys. 30, 182–189. Lilledahl, M., Pierce, D., Ricken, T., Holzapfel, G., de Lange Davies, C., 2011. Structural analysis of articular cartilage using multiphoton microscopy: input for biomechanical modeling. IEEE Trans. Med. Imaging 30 (9), 1635–1648.

Loparic, M., Wirtz, D., Daniels, A., Raiteri, R., vanLandingham, M., Guex, G., Martin, I., Aebi, U., Stolz, M., 2010. Micro- and nanomechanical analysis of articular cartilage by indentation-type atomic force microscopy: validation with a gel-microfiber composite. Biophys. J. 98, 2731–2740.

Lu, X., Mow, V., 2008. Biomechanics of articular cartilage and determination of material properties. Med. Sci. Sports Exerc. 40 (2), 193–199.

Lu, X., Wan, L., Guo, X., Mow, V., 2010. A linearized formulation of triphasic mixture theory for articular cartilage and its application to indentation analysis. J. Biomech. 43 (4), 673–679.

Nagel, T., Kelly, D., 2012. Mechanically induced structural changes during dynamic compression of engineered cartilaginous constructs can potentially explain increases in bulk mechanical properties. J. R. Soc. Interface 9 (69), 777–789.

Marondas, A., Wachtel, E., Grushko, G., Katz, E., Weimberg, P., 1991. The effect of osmotic and mechanical pressures on water partitioning in articular cartilage. Biochim. Biophys. Acta 1073 (2), 285–292.

Mow, V., Kuei, S., Lai, W., Armstrong, C., 1980. Biphasic creep and stress relaxation of articular cartilage in compression—theory and experiment. J. Biomech. Eng. 102, 73–84.

Mow, V., Zhu, W., Ratcliffe, A., 1991. Structure and function of articular cartilage and meniscus, Basic Orthopaedic Biomechanics. Raven Press, New York143–198.

Mow, V., Ratcliffe, A., Poole, A., 1992. Cartilage and diarthroidal joints as paradigms for hierarchical material and structure. Biomaterials 13 (2), 67–97.

Narmoneva, D., Wang, J., Setton, L., 1990. Nonuniform swelling-induced residual strains in articular cartilage. J. Biomech. 32, 401–408.

Nieminen, M., Rieppo, J., Toyras, J., Hakumaki, J., Silvennoinen, J., Hyttinen, M., Jurvelin, J., 2001. T2 relaxation reveals spatial collagen architecture in articular cartilage: a comparative quantitative MRI and polarized light micsoscopy study. Magn. Reson. Med. 46, 487–493.

Pierce, D., Trobin, W., Trattnig, S., Bischf, H., Holzapfel, G., 2009. A phenomenological approach toward patient-specific computational modeling of articular cartilage including collagen fiber tracking. J. Biomech. Eng. 131 (091006-1:12).

Pierce, D., Trobin, W., Raya, J., Trattnig, S., Bischof, H., Glaser, C., Holzapfel, G., 2010. DT-MRI based computation of collagen fiber deformation in human articular cartilage: a feasibility study. Ann. Biomed. Eng. 38 (7), 2447–2463.

Rice, J., Cleary, M., 1976. Some basic stress diffusion solution for fluid-saturated elastic porous media with compressible constituents. Rev. Geophys. Space Phys. 14, 227–241.

Schinagl, R., Gurskis, D., Chen, A., Sah, R., 1997. Depth-dependent confined compression modulus of full thickness bovine articular cartilage. J. Orthop. Res. 15 (4), 499–506.

Seifzadeh, A., Wang, J., Ouguamanam, D., Papini, M., 2011. A nonlinear biphasic fiber-reinforced porohyperviscoelastic model of articular cartilage incorporating fiber reorientation and dispersion. J. Biomech. Eng. 133 (081004-1:8).

Shapiro, E., Borthakur, A., Kaufman, J., Leigh, J., Reddy, R., 2001. Water distribution patterns inside bovine articular cartilage as visualized by 1H magnetic resonance imaging. Osteoarthr. Cartil. 9, 533–538.

Shirazi, R., Vena, P., Sah, R., Klisch, S., 2011. Modeling the collagen fibril network of biological tissues as a nonlinear elastic material using a continuous volume fraction distribution function. Math. Mech. Solids 16, 706–715.

Silver, F., Bradica, G., Tria Jr., A., 2003. Structure and biomechanics of articular cartilage. The Adult Knee, vol. I. Lippincott Williams & Wilkins, Philadelphia105–122.

Stender, M., Raub, C., Yamauchi, K., Shirazi, R., Vena, P., Sah, R., Hazelwood, S., Klisch, S., 2012. Integrating qPLM and biomechanical test data with an anisotropic fiber distribution model and predictions of TGF-β1 and IGF-1 regulation of articular cartilage fiber modulus. Biomech. Model Mechanobiol. 12 (6), 1073–1088.

Stolz, M., Gottardi, R., Raiteri, R., Miot, S., Martin, I., Imer, R., Staufer, U., Raducanu, A., Duggelin, M., Baschong, W., Daniels, A., Friederich, N., Aszodi, A., Aebi, U., 2009. Early detection of aging cartilage and osteoarthritis in mice and patient samples using atomic force microscopy. Nat. Nanotechnol. 4, 186–192.

Taffetani, M., 2013. Frequency and Time Domain Analysis on Fiber Reinforced Poroviscoelastic Tissue: Study on Articular Cartilage Through Nanoindentation Tests at Micrometric Characteristic Lengths. Politecnico di Milano (PhD dissertation).

Taffetani, M., Bertarelli, E., Gottardi, R., Raiteri, R., Vena, P., 2012. Modelling of the frequency response to dynamic nanoindentation of soft hydrated anisotropic materials: application to articular cartilage. Comp. Model. Eng. 87, 433–460.

Terzaghi, V., 1943. Theoretical Soil Mechanics. Wiley, New York.

Thomas, G., Asanbaeva, A., Vena, P., Sah, R., Klisch, S., 2009. A nonlinear constituent based viscoelastic model for articular cartilage and analysis of tissue remodeling due to altered glycosaminoglycan–collagen interactions. J. Biomech. Eng. 131 (10) 101002-1:11.

van der Voet, A., 1997. A comparison of finite element codes for the solution of biphasic poroelastic problems. Proc. Inst. Mech. Eng. H 211 (2), 209–211.

Vandamme, M., Ulm, F., 2006. Viscoelastic solution for conical indentation. Int. J. Solid Struct. 43, 3142–3165.

Wang, C., Deng, J., Ateshian, G., Hung, C., 2002. An automated approach for direct measurement of two-dimensional strain distributions within articular cartilage under unconfined compression. J. Biomech. Eng. 124, 557–567.

Wilson, W., van Donkelaar, C., van Rietbergen, B., Cohen, I., 2005. A fibril reinforced poroviscoelastic swelling model for articular cartilage. J. Biomech. 38, 1195–1204.

Wilson, W., van Donkelaar, C., van Rietbergen, B., Ito, K., Huiskes, R., 2004. Stresses in the local collagen network of articular cartilage: a poroviscoelastic fibril reinforced finite element study. J. Biomech. 37, 357–366.